Coupling 1-D Arterial Blood Flow to 3-D Tissue Perfusion Models for In Silico Trials of Acute Ischaemic Stroke

Padmos, Raymond.M.[1], Józsa, Tamás.I.[2], El-Bouri, Wahbi.K.[2], Payne, Stephen.J.[2], Hoekstra, Alfons.G.[1]

[1]Computational Science Laboratory, Institute for Informatics, Faculty of Science, University of Amsterdam, Science Park 904, Amsterdam 1098 XH, The Netherlands

[2]Institute of Biomedical Engineering, Department of Engineering Science, University of Oxford, Parks Road, Oxford OX1 3PJ, UK

1 Abstract

An acute ischaemic stroke is due to the sudden blockage of an intracranial blood vessel by an embolised thrombus. In the context of setting up in-silico trials for the treatment of acute ischaemic stroke, the effect of a stroke on perfusion and metabolism of brain tissue should be modelled to predict final infarcted brain tissue. This requires coupling of blood flow and tissue perfusion models. A 1-D intra cranial blood flow model and a method to couple this to a brain tissue perfusion model for patient-specific simulations is presented. Image based patient-specific data on the anatomy of the circle of Willis is combined with literature data and models for vessel anatomy not visible in the images to create an extended model for each patient from the larger vessels down to the pial surface. The coupling between arterial blood flow and tissue perfusion occurs at the pial surface through the estimation of perfusion territories. The coupling method is able to accurately estimate perfusion territories. Finally, we show that blood flow can be approximated as steady state flow at the interface between arterial blood flow and tissue perfusion to reduce the cost of organ-scale simulations.

2 Keywords:

1-D blood flow model, Perfusion territories, cerebral perfusion, acute ischemic stroke

3 Introduction

An acute ischaemic stroke is the most common type of stroke. It is fatal to an estimated three million people globally every year and may lead to a dramatic loss of quality of life in survivors (1). An acute ischaemic stroke occurs when blood supply to the brain is suddenly blocked by an embolised thrombus. This results in the acute loss of blood flow to downstream vessels. Consequently, brain tissue is starved of oxygen resulting in necrosis causing disability and ultimately death. Currently only a few treatment options exist. Improving existing treatments and developing and approving new treatments is a difficult, lengthy, and expensive process, prone to failures during clinical trials even after successful animal trials.

The INSIST project[1] (2) aims to develop computational models that will be used to simulate a clinical stroke trial on a virtual population. The (virtual) patient in this context is generally a set of parameters and other data that is used in a computational model. In silico trials (IST) can overcome some of the limitations of clinical trials, lower their cost, contribute to developing more efficient clinical trials, or shorten the preclinical trajectories (3). IST are closely related to computational biomedicine or personalized medicine. The goal is to predict the efficacy and efficiency of a treatment, drug or device. As such they are similar to normal clinical trials where the testing happens on animals or humans. Computational modelling has become the standard in many industries from the design of air planes to electronics. Likewise, computational models in the medical field are slowly gaining momentum (4–9).

One of the goals of INSIST is to predict the location and volume of the infarcted brain tissue for stroke patients both for individual patients and at the population level. This requires modelling blood flow across length scales incorporating three orders of magnitude, from the large arteries via the arterioles and the pial surface vessels to the penetrating vessels and the microcirculation deep in the brain. Blood flow in large vessels are typically modelled using lumped parameter or 1-D blood flow models, whereas the microcirculation is typically modelled as a porous medium (10). In addition, there is limited knowledge about the vessel anatomy between the large vasculature and the microcirculation. Data of the intermediate vessels are limited or only available as statistical scaling laws. Predicting infarcted volume requires thus the coupling of arterial blood flow models to tissue perfusion models. A tissue perfusion model is presented in another article in this same special issue of Interface Focus (11). A 1-D blood flow model has to be coupled to this tissue perfusion model, which presents several challenges.

Firstly, medical images often suffer from low resolution. Scans from stroke patients are often done quickly to get an assessment of the stroke severity. As a result, the scans typically only contain the circle of Willis and a few of the major cerebral arteries, see Figure 2a. This presents a problem as this does by far not provide sufficient information for the coupling between arterial blood flow and tissue perfusion. However, there are high resolution scans available from different individuals (12,13). Unfortunately, this dataset, referred to as the BraVa dataset, does not contain other information such as pressure, heart rate, Young's modules etc.

Secondly, information about the perfusion territories of the cerebral arteries can be determined but is limited (14). The perfusion territory of a blood vessel is the region of tissue that receives blood from that vessel. Not much is known about the perfusion territories of the brain and data are again sparse. Coupling blood flow to tissue perfusion in a patient-specific manner requires the estimation of the perfusion territory for every perfusing vessel.

---

[1] www.insist-h2020.eu

Here, a method is presented to couple blood flow in cerebral blood vessels to cerebral tissue perfusion. Patient-specific image-based vessel segmentations are combined with literature data and models for vessel anatomy not visible in the images to create an extended model for each patient. Using Murray's law, we estimate perfusion territories on the pial surface using a coupling algorithm. Arterial blood flow is simulated with a 1-D pulsatile blood flow model with three-element windkessel elements at the boundaries. We show that at the pial surface, blood flow pulsatility is small and blood flow can be approximated as steady state flow.

4 Methods

4.1 Vasculature of Virtual Patients

Vessel centrelines are extracted from vessel segmentations of CT angiographs from stroke patients entering the hospital. The centrelines contain the Circle of Willis (CoW) and the side branches, see Figure 1a. The side branches are the posterior cerebral artery (PCA), anterior cerebral artery (ACA) and middle cerebral artery (MCA). This patient-specific vasculature is first extended with the larger vessels, starting from the heart, see Figure 1b. The smaller vessels to the cerebellum and brainstem are also added. The default parameters describing these arteries are taken from literature (15,16) and are shown in Table 1.

Table 1: Default values for large vessels, adapted from (15,16).

Vessel Name	Length (mm)	Proximal Radius (mm)	Distal Radius (mm)	Young's modulus (MPa)
Ascending Aorta	40	12	12	0.4
Aortic Arch I	20	11.2	11.2	0.4
Brachiocephalic	34	6.2	6.2	0.4
Aortic Arch II	39	11	11	0.4
L. common carotid	208	2.5	2.5	0.4
R. common carotid	177	2.5	2.5	0.4
R. subclavian	34	4.23	4.23	0.4
Thoracic aorta	156	9.99	9.99	0.4
L. subclavian	34	4.23	4.23	0.4
L ext. carotid	177	1.5	1.5	0.8
L int. carotid I	177	2	2	0.8
R int. carotid I	177	2	2	0.8
R ext. carotid	177	1.5	1.5	0.8
R. vertebral	148	1.36	1.36	0.8
R. brachial	422	4.03	4.03	0.4
L. brachial	422	4.03	4.03	0.4
L. vertebral	148	1.36	1.36	0.8
L. PCoA	15	0.73	0.73	1.6
R. PCoA	15	0.73	0.73	1.6
Basilar I	5.6	1.62	1.62	1.6
L. MCA	119	1.43	1.43	1.6

|				
R. MCA	119	1.43	1.43	1.6
L. ACA, A1	12	1.17	1.17	1.6
R. ACA, A1	12	1.17	1.17	1.6
L. PCA, P1	5	1.07	1.07	1.6
R. PCA, P1	5	1.07	1.07	1.6
L. ACA, A2	103	1.2	1.2	1.6
R. ACA, A2	103	1.2	1.2	1.6
ACoA	3	0.74	0.74	1.6
L. PCA, P2	86	1.05	1.05	1.6
R. PCA, P2	86	1.05	1.05	1.6
R. SCA	10	0.78	0.78	1.6
L. SCA	10	0.78	0.78	1.6
R. AICA	10	0.63	0.63	1.6
L. AICA	10	0.63	0.63	1.6
Basilar II	5.6	1.62	1.62	1.6
Pontine I	5	0.2	0.2	1.6
Pontine II	5	0.2	0.2	1.6
Pontine III	5	0.2	0.2	1.6
Pontine IV	5	0.2	0.2	1.6
Pontine V	5	0.2	0.2	1.6
Pontine VI	5	0.2	0.2	1.6
Pontine VII	5	0.2	0.2	1.6
Pontine VIII	5	0.2	0.2	1.6
Pontine IX	5	0.2	0.2	1.6
Pontine X	5	0.2	0.2	1.6
Pontine XI	5	0.2	0.2	1.6
Pontine XII	5	0.2	0.2	1.6
Basilar III	5.6	1.62	1.62	1.6
Basilar IV	5.6	1.62	1.62	1.6
Basilar V	5.6	1.62	1.62	1.6
R. PICA	10	0.63	0.63	1.6
L. PICA	10	0.63	0.63	1.6
R. vertebral II	20	1.36	1.36	0.8
L. vertebral II	20	1.36	1.36	0.8
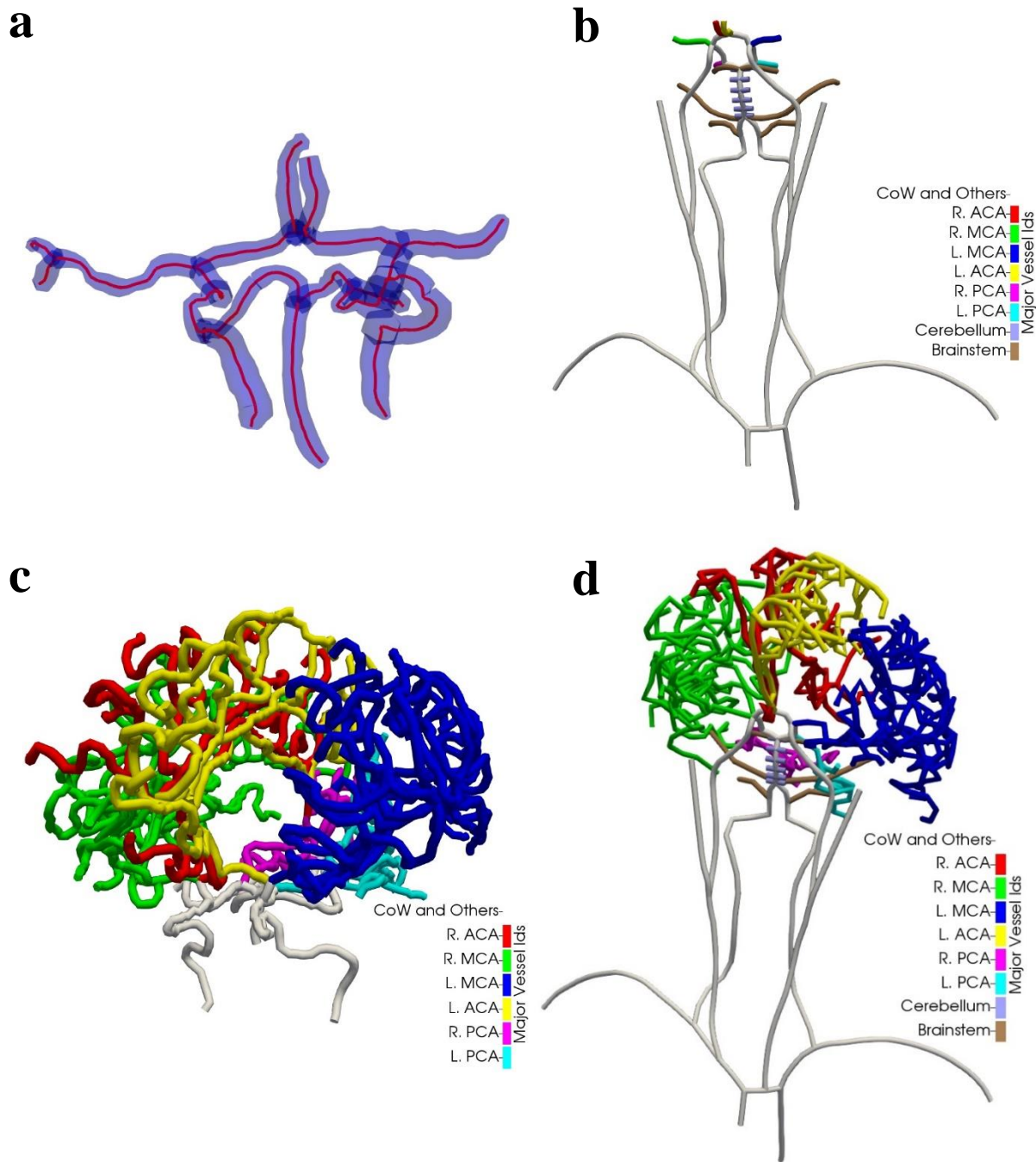
Figure 1: (a) Segmentation from a CT angiography from a stroke patient in blue. The segmentation contains the circle of Willis and several side branches. Centrelines are extracted and shown in red. (b) the large arteries, starting from the heart leading up to and including the patient specific circle of Willis. Smaller vessels to the brain stem and cerebellum are also included. Note that the vessels are not drawn to scale. (c) One of the centreline segmentations from the BraVa dataset (ID: BG18). Each vessel is smoothed by setting the radius at every point to the mean radius of that vessel. Vessels are colour coded according to which major cerebral vessel they belong. The circle of Willis vessels from the BraVa segmentation are not used and are replaced by the patient-specific circle of Willis from a. (d) The final patient-specific arterial network. Patient-specific data from 1a are extended with literature values from

b and high-resolution data from c. This is the network that is used in the 1-D blood flow simulations. Note that the vessels are not drawn to scale.

Centrelines of high resolution scans of cerebral arteries are available from 61 different individuals (12,13). These centrelines are referred to as the BraVa dataset. The arteries in the datasets are labelled by six major cerebral arteries from which they emerged, i.e. left and right ACA, MCA and PCA, and the CoW, see Figure 1c. One segmentation of the BraVa set is randomly chosen and attached to the patient specific vasculature. For each major cerebral artery in the patient vasculature, the equivalent vessel in the BraVa vasculature is used as an attachment point. The radii of the added vessels are scaled by the ratio of equivalent cerebral vessels, ACA, MCA, PCA etc, between the BraVa dataset and the patient specific vasculature. All radii are scaled to preserve any scaling law between the vessels.

These three sets of data are combined to create a patient-specific vasculature that starts at the heart and ends close to the pial surface. For each major cerebral artery in the patient dataset, the relevant vessels in the Brava dataset are identified and then attached to each other. On the other end of the patient anatomy, the large arteries to the heart are connected, see Figure 1d.

4.2   1-D Blood Flow Modelling

1-D blood flow models (17–23) are able to model blood flow in sufficient detail without becoming too computationally expensive. Blood flow is modelled as a viscous incompressible fluid. Vessels are modelled as elastic tubes with a taper. Blood flow is assumed to be rotationally symmetric around the centreline of the vessel. Following (17,20), the continuity of mass and momentum equations are obtained by integrating the Navier-Stokes equations over two dimensions, resulting in

$$\frac{\partial \bar{v}_x}{\partial t} + (2\alpha - 1)\bar{v}_x \frac{\partial \bar{v}_x}{\partial x} + (\alpha - 1)\frac{\bar{v}_x^2}{A}\frac{\partial A}{\partial x} + \frac{1}{\rho}\frac{\partial p}{\partial x} = \frac{-2\alpha\mu\pi\bar{v}_x}{(\alpha - 1)\rho A}, \tag{1}$$

$$\frac{\partial A}{\partial t} + \frac{\partial (A\bar{v}_x)}{\partial x} = 0, \tag{2}$$

with

$$p = p_{ext} + \frac{\beta}{A_0}\left(\sqrt{A} - \sqrt{A_0}\right), \tag{3}$$

$$\beta = \frac{\sqrt{\pi}Eh}{(1 - v^2)}, \tag{4}$$

and where $\bar{v}_x$ is the average velocity, α is a momentum correction factor, A is the cross-sectional area, A_0 is the initial area, p is the pressure, μ is the dynamic viscosity, ρ the density of blood, p_{ext} is a reference pressure, E is the Young's modules, and v is the Poisson ratio.

Vessels are linked together at bifurcations by the method of characteristics (17–23). The method used here to solve the resulting equations is the MacCormack method, a second-order finite difference method. The initial conditions are zero velocity and diastolic pressure everywhere. Every vessel has a minimum of three nodes and a maximum separation of 10mm. The simulation is run for a small number of heart beats and iterated until the tolerance between iterations is below a threshold, defined as

$$\frac{|\overrightarrow{p_i} - \overrightarrow{p_{i-1}}|}{|\overrightarrow{p_i}|} < 10^{-3} \tag{5}$$

with $\overrightarrow{p_i}$ being a vector of the pressure at all nodes at all times during the i-th cardiac cycle and $\overrightarrow{p_{i-1}}$ a vector of the pressure at the previous iteration $i - 1$. The typical number of simulated cardiac cycles before convergence is below 10.

The heart provides the inlet boundary conditions to the model while a three-element windkessel model is used at each outlet. Note that the BraVa anatomies typically have in the order of 100 outlets. Volume flow rate at the inlet is given by an inlet function and taken from Boileau et al (21). The inlet function is scaled based on stroke volume and heart rate for each patient. The total resistance and compliance of the full vascular tree model is calculated by (24)

$$R_{tot} = \frac{\frac{1}{3}P_{sys} + \frac{2}{3}P_{dia}}{SV * HR} \tag{6}$$

and

$$C_{tot} = \frac{\tau}{R_{tot}} \tag{7}$$

with P_{sys} the systolic pressure, P_{dia} the diastolic pressure, SV the stroke volume, HR the heart rate and τ the aortic pressure decay time constant. The compliance of the patient network is calculated from the sum of the vessel compliances given by

$$C_{1D} = \frac{3A\sqrt{A}L}{2\sqrt{\pi}Eh} \tag{8}$$

where A is the area, L is the length, E is the Young's modules and h is the thickness of the vessel. The thickness of the vessel is calculated using an empirical function given by

$$h = R_0[a\exp(bR_0) + c\exp(dR_0)] \tag{9}$$

with R_0 the initial radius, $a = 0{,}2802$, $b = $ -5,053cm^{-1}, $c = 0{,}1324$ and $d = $ -0,1114cm^{-1} (23). The network compliance is substantial for large vessel and is therefore subtracted from the total compliance. The resistance of the patient network is assumed to be negligible for the large arteries compared to the total resistance.

Known distributions of cardiac output into the main vessels are used to distribute the resistance and compliance to each outlet. That is, 65% goes to the lower body through the Thoracic aorta, 5% goes to the arms through the left and right Brachial, and the rest to the other outlets. The resistance and compliance are distributed to the outlets, R_T and C, based on the fraction of the radius cubed, e.g. Murray's law (25)

The total resistance of the attached cerebral arteries is subtracted to account for the resistance added by the attachment of the BraVa vessels to the patient network. The resistance of the added vasculature is calculated by iteratively adding resistances depending on whether vessels run in parallel or serial. The two resistance windkessel parameters, R_1 and R_2, of each outlet are calculated by:

$$R_1 = \frac{\rho}{A_0}\sqrt{\frac{2Eh}{3\rho R_0}} \tag{10}$$

$$R_2 = R_T - R_1 \tag{11}$$

The choice for R_1 leads to the minimization of unnatural wave reflections at the outlets (26). The outlets of the 1-D blood flow model provide blood flow to the perfusion territories of the brain. A stroke is modelled as a complete blockage of flow and pressure by enforcing Neumann pressure boundary conditions at the boundary of the clot. The default parameters of the model are listed in Table 2.

The extension process proceeds along the following steps:

1. Identify identical vessels in both datasets by their label;
2. Extract the smaller upstream vessels starting from the major cerebral artery;
3. Calculate the mean radius for identical vessels in both datasets;
4. Scale the radii of the upstream vessels identified previously accordingly;
5. Attach the upstream vessels to the relevant end in the patient vasculature;
6. Calculate the resistance of the appended vessels;
7. Subtract the resistance and distribute the remainder to the appended ends.

Table 2: Default model parameters

Parameter	Value
Density	1050 kg m^{-3}
Viscosity	0.0035 Pa s
Venous Pressure	2500 Pa
Heart Rate	60 min^{-1}
Systole Pressure	17300 Pa
Diastole Pressure	10100 Pa
Stroke Volume	70 mL
Momentum correction factor	1.1
Aortic pressure decay time	1.34 s
Poisson ratio	0.5

To characterise the strength of the pulsatility of blood flow, pulsatility indices are used. The pressure pulsatility index is given by

$$Pi_p = \frac{p_{max} - p_{min}}{p_{mean}} \tag{12}$$

with p_{max} the maximum pressure, p_{min} the minimum pressure, and p_{mean} the mean pressure. The velocity pulsatility index is given by

$$Pi_v = \frac{v_{max} - v_{min}}{v_{mean}} \tag{13}$$

with v_{max} the maximum velocity, v_{min} the minimum velocity, and v_{mean} the mean velocity.

4.3 Estimating Perfusion Territories

Coupling blood flow to tissue perfusion in a patient-specific manner requires the estimation of the perfusion territory for every perfusing vessel, so for every outlet of the BraVa sets (i.e left and right ACA, MCA and PCA), the Cerebellum and the brainstem. Using Murray's law,

perfusion territories on the pial surface are estimated using a coupling algorithm. The radius of the outlet is assumed to be related to the perfusion of tissue by Murray's law given by

$$r_i^3 \propto Q_i \tag{14}$$

with r_i^3 the cubic radius at outlet i and Q_i the volume flow rate at outlet i.

We estimate the fraction of the pial surface that belongs to each outlet i of the patient vasculature at the pial surface with the use of Murray's law. This fraction is calculated as

$$f_i = \frac{Q_i}{\sum_{j=0}^{n} Q_j} = \frac{r_i^3}{\sum_{j=0}^{n} r_j^3} \tag{15}$$

with Q_i the volume flow rate at the outlet and r_i^3 the cubic radius at the outlet. The volume flow rate per area, or flow velocity, is uniform over the pial surface under these assumptions. To what extend this is also true for a real brain is not clear.

The pial surface is represented as a uniform triangulated mesh, Figure 2a, where each triangle represents an equal sized area on the mesh. The mesh was presented in the study of Garcia-Gonzalez et al where it was used for finite element computations (27). The triangles are grouped based on distance, calculated with Dijkstra's algorithm, using a coupling algorithm, Figure 2b and 2c. The number of surface elements that belongs to each outlet is calculated by

$$n_i = f_i N_{Tot} \tag{16}$$

with N_{Tot} the number of triangles of the uniform triangulated mesh.

The coupling algorithm ensures that the size of the perfusion territories is scaled based on the cubed radius of vessel that perfuses it, i.e. Murray's law. After the coupling, any unassigned surface elements are assigned to the nearest cluster. The surface elements are assigned to the nearest outlet based on their separation on the surface. This is an iterative algorithm to account for the mismatch between the pial surface and the outlet. The outlet position is updated by taking the centre point of the assigned surface elements as a new guess. The new centre point is determined by minimizing the maximum separation between points.

Data from vessel encoded arterial spin labelling (VEASL) is used to confine the sampling of the mesh to regions that belong to the same major cerebral vessel (28–30). This is done to achieve a better match between the estimated area and area of the surface mesh. The pial surface mesh does not contain the complex folding of the brain nor does it contain well separated frontal and temporal lobes. By using VEASL data, the mismatch between the expected area and the area of the surface mesh can be limited to the major territories of the brain. The major territories of the brain are the left and right ACA, MCA and PCA, the Cerebellum and the brainstem. Vessels perfusing the pial surface are confined to the equivalent regions in the VEASL data. The coupling algorithm tries to find the sets for which the sum of distances within the set of surface elements is minimal. Note that the cluster sizes are calculated beforehand using equation 16.
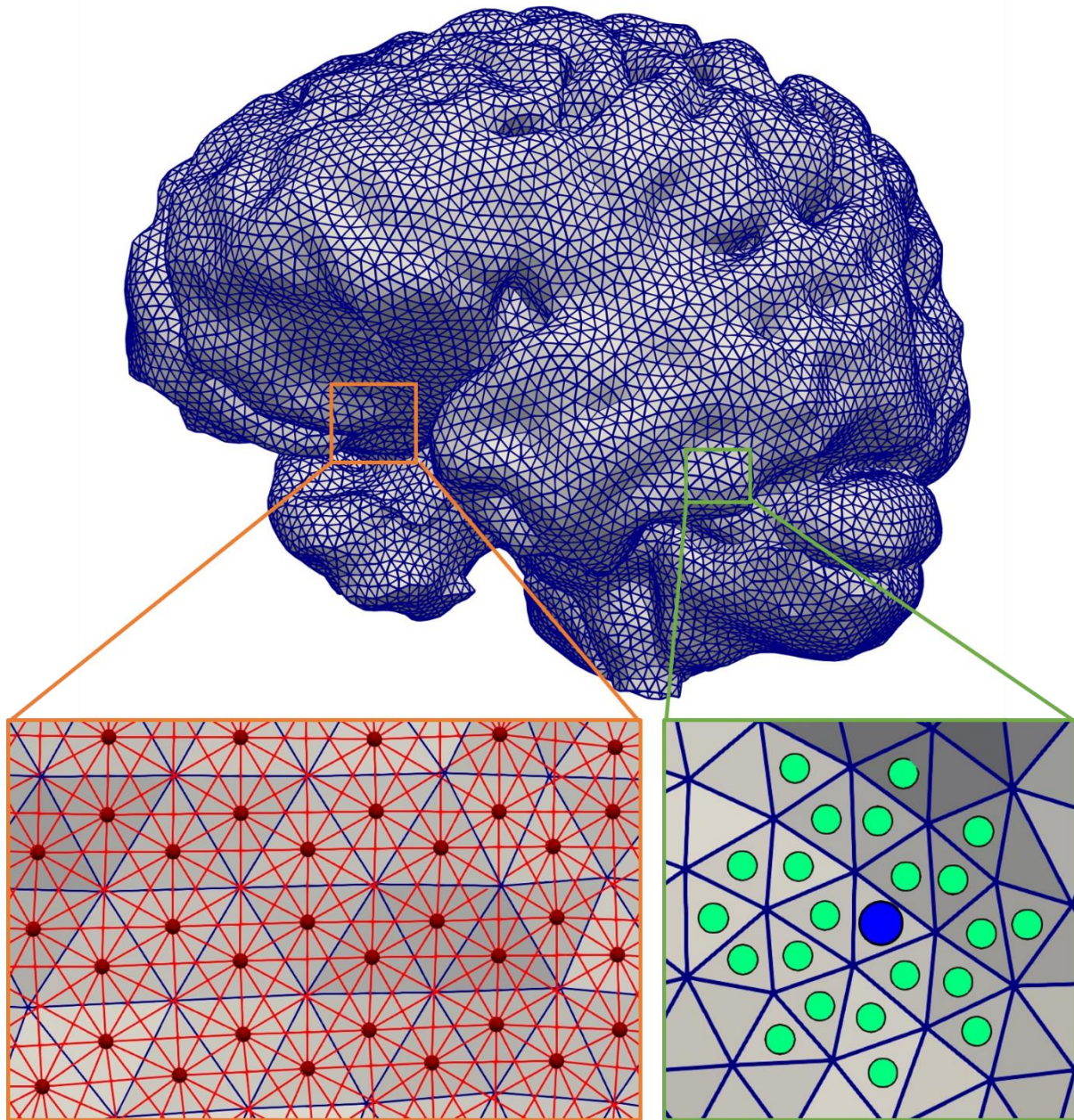
Figure 2: (a) The pial surface as a uniform triangulated mesh. (b) Nodes are the centres of the triangles from a, shown as red circles, and connected by red lines if they share a vertex. The distance between connected nodes is the Euclidean distance. (c) The outlet of a vessel is projected to the surface, blue circle. The nearest surface elements, i.e. triangles, are assigned to the nearest outlet, green circles. Distance between surface elements is determined by Dijkstra's algorithm from the graph in b.

The root of the perfusion territories can be thought of as the mean position of the surface elements in that set. The surface is transformed into a graph and Dijkstra's distance algorithm is used, Figure 2b. Euclidean distance can also be used if the surface is relatively flat. The pseudo code is given by:

1. Determine the number of surface elements per outlet with equation 16
2. Project the outlet to the pial surface as an initial guess for the root

3. Find the closest set of elements to the root
4. Minimize the root-element distance within the clusters
5. Update the root
6. Iterate until convergence
7. Repeat for each major cerebral region.

The mean flow velocity at outlets of the blood flow model is distributed evenly across the relevant perfusion territory. Each triangle of the mesh receives a volume flow rate based on its fractional area such that the flow velocity, i.e. volume flow rate per area, is uniform within each perfusion territory and within the major region set by the VEASL data. The result of the coupling is shown in Figure 4, error estimation in Figure 5 and blood flow at the pial surface in Figure 6.

5 Results and Discussion

Extending patient-specific data on the anatomy of the circle of Willis with high-resolution data from the BraVa sets and literature can solve some of the problems of missing vessels. We include the arteries starting at the heart such that we can capture the redirection of flow in the event of a stroke. This is often excluded from many models that look at stroke. For large vessel occlusions, it is likely that the redistribution of blood can have significant effects on perfusion. A more detailed study on this is underway and will be reported elsewhere.

The extended patient vasculature, Figure 1d, should contain sufficient detail to capture all relevant effects such as the redistribution of flow after a stroke and make it possible to model volume flow rates, pressure and other variables. Once the patient anatomy is extended to the smaller cerebral arteries, we can begin to map the flow in the arteries to the brain. Modelling the entire cerebral vasculature down to the microcirculation is too computationally expensive and probably also not required for our purpose. Being able to switch to a more efficient model is therefore crucial. The 1-D blood flow model used in this paper is commonly used, well studied and validated. The outlets of the 1-D blood flow model provide blood flow to the perfusion territories of the brain.

Statistically accurate vessel networks can be generated between the outlets of the BraVa sets and the coupling points at the pial surface (Figure 1c) using constrained constructive optimization (31–33). However, one of the underlying assumptions of such algorithms is that the radii at the terminal points are equal and their positions are randomly chosen within a target volume. Since the assumption here is that there is no seepage through the vessel wall, the volume flow rates at the outlets would all be equal for a symmetric bifurcating tree. Simple scaling laws, such as Murray's law and a length-to-radius ratio, can be used to generate bifurcating trees as the 1-D blood flow model only depends on the length and the radius and not the position of the vessels.

Pulsatile blood flow was simulated in the anatomy of Figure 1d, using parameters from table 2. The simulations where performed for seven heartbeats, after which the solution converged. Time dependent volume flow and pressure along the anatomy was obtained, and from that both velocity and pressure pulsatility indices were computed.
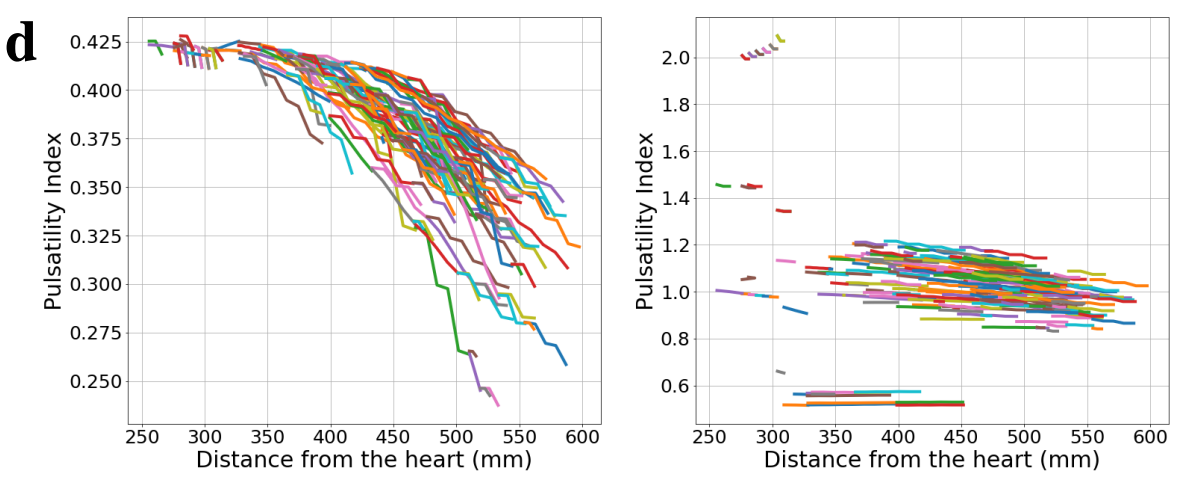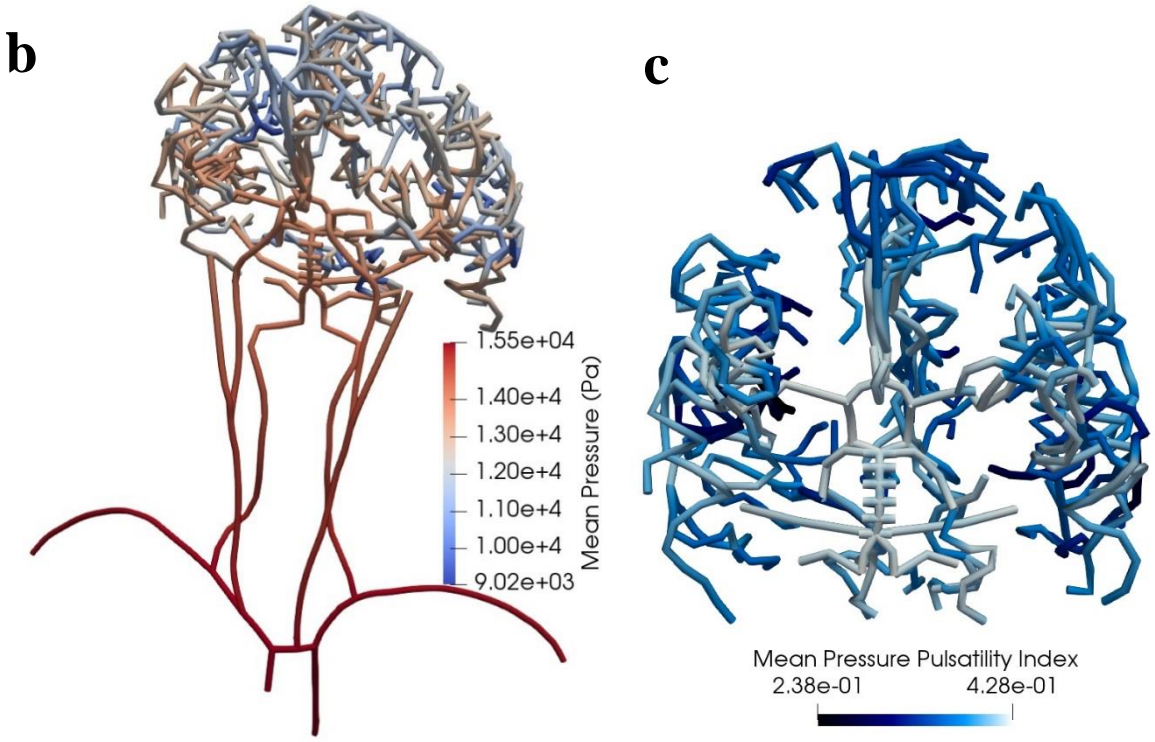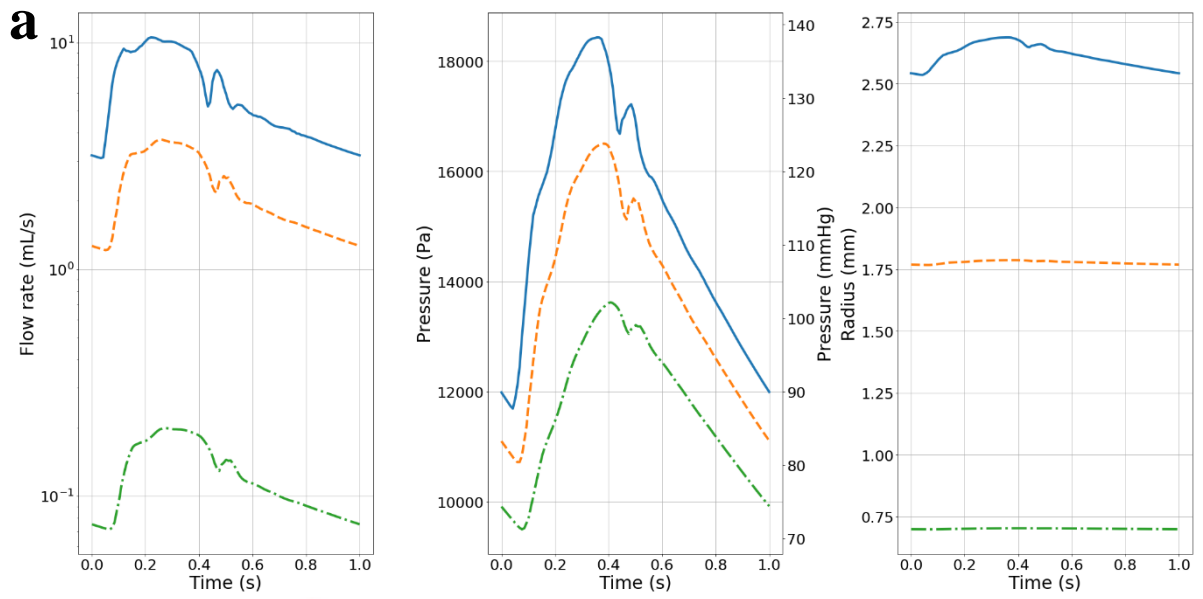
Figure 3: (a) Results from the 1-D blood flow simulation for three different locations in the vasculature. The volume flowrate, pressure and radius over time are plotted. The locations are chosen based on their size. The chosen vessels were the right common carotid artery, the right middle cerebral artery and one outlet vessel belonging to the right middle cerebral vasculature. (b) Mean pressure for the patient-specific vasculature calculated by the 1-D blood flow model. Note that the vasculature shown here is mapped to a 3-D anatomy that is the same for all patients and is used only for visualisation, the length and radii are not to scale. (c) Pressure pulsatility index in the patient-specific vasculature of the CoW and downstream vessels. (d) Pressure and velocity pulsatility indices as a function of distance from the heart. Each line represents an individual vessel. Only vessels belonging to the CoW and beyond are shown.

The pulsatility decreases as a function of distance from the heart for most vessels. Pulse pressure amplification is observed at the brachial arteries. Figure 3a shows the volume flow rate, pressure and radius of three vessels at different sizes, one large, one intermediate and one small artery. The chosen vessels were the right common carotid artery, the right middle cerebral artery and one outlet vessel belonging to the right middle cerebral vasculature. The figure shows that the volume flow rate profile only changes in magnitude as the flow is split at every bifurcation. The pressure profile changes as the higher frequencies are damped. The vessel radius changes depending on the pressure and the properties of the vessel. The radii of the small cerebral arteries do not change much. The cerebral vessels are much stiffer than the large arteries and the pressure is lower further away from the heart, see Figure 3b (34).

Figure 3c shows the velocity PI in the cerebral vasculature. Figure 3d shows the pressure and velocity PIs as function of distance from the heart. Measurements of the pulsatility index of the right middle cerebral artery are possible through transcranial Doppler ultrasound. The PI measured is often the velocity PI also known as Gosling's pulsatility index (35). PI is thought to reflect the downstream vascular resistance and changes in PI are associated with various diseases (36,37).

Table 3 shows the pulsatility indexes for the middle cerebral artery. Comparing the values found to those in literature shows that the model overestimates the velocity PI (36,38,39). Stiffness of the vessels play an important role in the transmission of pulsatility through the vasculature (40). Obtaining patient-specific Young's moduli for every vessel is difficult and can explain the overestimation of the velocity PI in the model. Pressure pulsatility index decreases more than the velocity pulsatility index as a function of distance from the heart. This is likely due to the dampening seen in the pressure profiles, see Figure 3a. This suggests that the pressure PI is a better measure of the downstream resistance than the velocity PI.

Table 3: Velocity pulsatility index of the MCA.

Origin	Mean (SD)
Model (default anatomy)	1.02
Model with patient data	1.08
(38)	0.754 (0.110) (Women) 0.823 (0.154) (Male)
(39)	0.74 (0.04)
(36)	0.86 (0.18)

The pulsatility decreases as the radius of the vessel decreases. see Figure 3c and 3d. High frequencies are effectively decreased in magnitude. The pressure pulsatility index shows that there are two types of behaviour. The first type is the pulse pressure amplification in the

brachial arteries. The second type is the slow decrease in pulsatility index as distance from the heart increases. Velocity pulsatility seems to reach a minimum at around one. Changes in volume flow rate become negligible on the timescale of tissue oxygenation and cell death. We therefore argue that we can approximate the volume flow rates at the pial surface as steady state flow. The mean volume flow rate over the region does not depend on details of the vasculature due to conservation of mass. The steady state only changes due to a major event in the vasculature such as a stroke. We therefore map the mean volume flow rate directly from the vessel outlet to its perfusion territory. One could go further and replace the entire blood flow model with a steady state resistance model.

Tables 3 and 4 show the mean PI and mean volume flow rates for the model with and without patient segmentations used to personalize the model. The configuration of the CoW and the stroke itself will change the outcome such that we cannot compare the model output to values from literature for healthy patients. Note that the model is not calibrated nor fitted to match the reference values. The pulsatility indices when compared to the refence value do seem to be too high but without either calibration nor sufficient patient data, this is unsurprisingly. Getting correlated high-quality data for stroke patients is difficult. This is something that we hope to address in future work.

Table 4: Volumetric flow rates (mL/min) per vessel for the model with and without patient segmentations.

Vessel	Model (patient)	Model (default)
Ascending Aorta	4.20E+03	4.20E+03
Aortic Arch I	3.53E+03	3.54E+03
Brachiocephalic	6.76E+02	6.61E+02
Aortic Arch II	3.15E+03	3.19E+03
L. common carotid	3.80E+02	3.47E+02
R. common carotid	3.67E+02	3.57E+02
R. subclavian	3.05E+02	3.03E+02
Thoracic aorta	2.84E+03	2.89E+03
L. subclavian	3.05E+02	3.03E+02
L ext. carotid	8.64E+01	1.47E+02
L int. carotid I	2.92E+02	1.98E+02
R int. carotid I	2.80E+02	2.09E+02
R ext. carotid	8.71E+01	1.48E+02
R. vertebral	8.82E+01	8.20E+01
R. brachial	2.17E+02	2.21E+02
L. brachial	2.17E+02	2.21E+02
L. vertebral	8.83E+01	8.21E+01
L. PCoA	-8.35E+00	1.30E+01
R. PCoA	5.65E+01	1.37E+01
Basilar I	1.50E+02	1.16E+02
L. MCA	1.93E+02	1.22E+02
R. MCA	1.35E+02	1.25E+02
L. ACA, A1	1.08E+02	6.24E+01

R. ACA, A1	8.95E+01	6.92E+01
L. PCA, P1	-6.73E+01	-3.48E+01
R. PCA, P1	-5.65E+01	-3.27E+01
L. ACA, A2	1.08E+02	6.30E+01
R. ACA, A2	8.92E+01	6.96E+01
ACoA	-	1.28E-01
L. PCA, P2	5.89E+01	4.82E+01
R. PCA, P2	1.13E+02	4.69E+01
R. SCA	1.20E+01	2.22E+01
L. SCA	1.20E+01	2.22E+01
R. AICA	6.46E+00	1.18E+01
L. AICA	6.46E+00	1.18E+01
Basilar II	1.50E+02	1.15E+02
Pontine I	2.06E-01	3.76E-01
Pontine II	2.05E-01	3.74E-01
Pontine III	2.04E-01	3.73E-01
Pontine IV	2.03E-01	3.72E-01
Pontine V	2.02E-01	3.71E-01
Pontine VI	2.02E-01	3.70E-01
Pontine VII	2.06E-01	3.76E-01
Pontine VIII	2.05E-01	3.74E-01
Pontine IX	2.04E-01	3.73E-01
Pontine X	2.03E-01	3.72E-01
Pontine XI	2.02E-01	3.71E-01
Pontine XII	2.02E-01	3.70E-01
Basilar III	1.49E+02	1.14E+02
Basilar IV	-1.49E+02	-1.14E+02
Basilar V	-1.48E+02	-1.13E+02
R. PICA	6.56E+00	1.20E+01
L. PICA	6.56E+00	1.20E+01
R. vertebral II	8.02E+01	6.89E+01
L. vertebral II	8.03E+01	6.90E+01

The coupling algorithm is able to consistently map the outlets of the blood flow model to the pial surface. The coupling method works with any pial surface mesh and a higher resolution mesh will also increase the resolution of the perfusion territories. The choice of BraVa subject does not affect the blood flow variables before the CoW with the coefficient of variation not exceeding 0.005 for any vessel in Table 1. However, there is variation in the location and size of the perfusion territories. This is likely to reflect the individuality of the cerebral vasculature. Computation times for the 1-D blood flow simulation are on the order of 10 minutes while the coupling algorithm takes significantly more time and are on the order of 60 minutes. Computations are done on a standard desktop computer with an Intel core i7-7700k running at 4.2GHz with 16GB RAM.

Figure 4a shows the mapping of the pial surface based on the major artery from which the vessels originate. To date, only the perfusion territories for the major cerebral arteries are well-

established (14,41). The major cerebral perfusion territories are enforced with the use of VEASL data. This is done to try to limit the error between the expected area and the area on the surface mesh. The surface mesh does not capture all the complex folding of the brain and a mismatch is expected. This lack of resolution is a serious limitation of the coupling algorithm. A downside of this is that the fractional areas, equation 15, are only strictly valid within each region, see Figure 5.
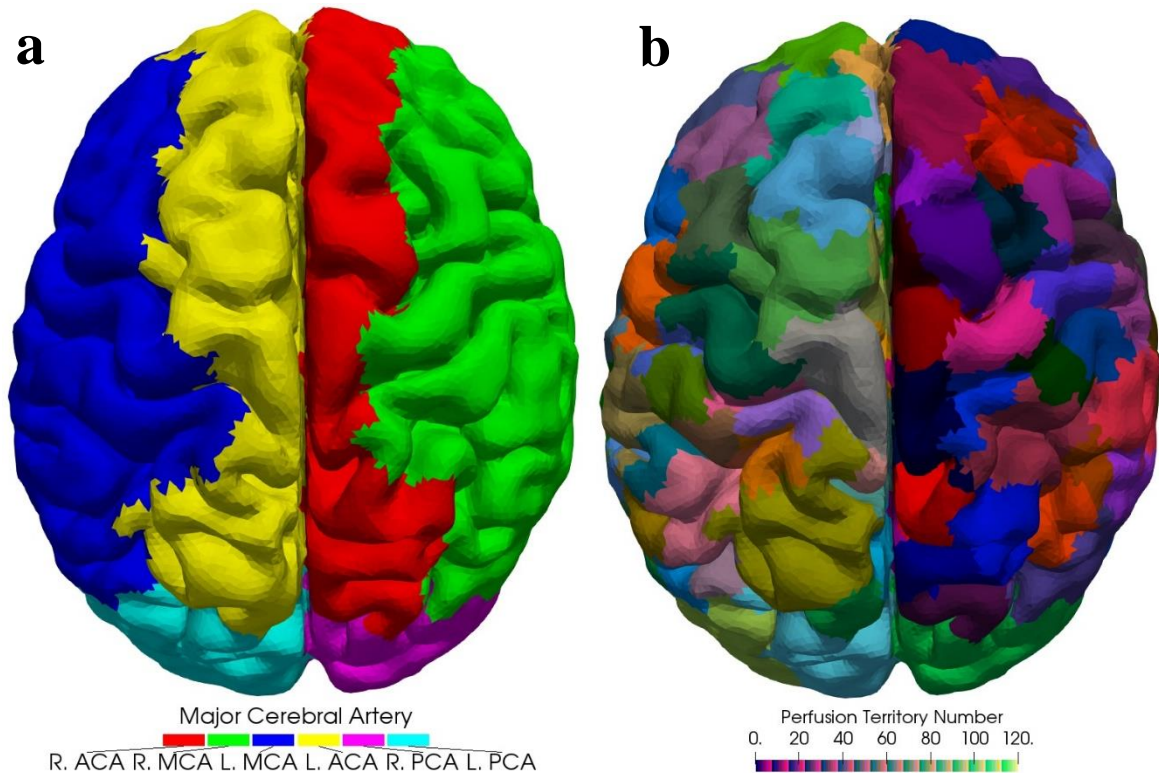

Figure 4: (a) The pial surface mapped by the coupling algorithm. The major region id for each triangle of the pial surface mesh is shown. Note that this result is enforced by the algorithm. (b) The pial surface mapped by the coupling algorithm. Each triangle is coloured based on the cluster id. Each coloured region corresponds to one outlet of the 1-D blood flow model. Each cluster is one connected region and lies within its major cerebral vessel domain as shown in figure (a).
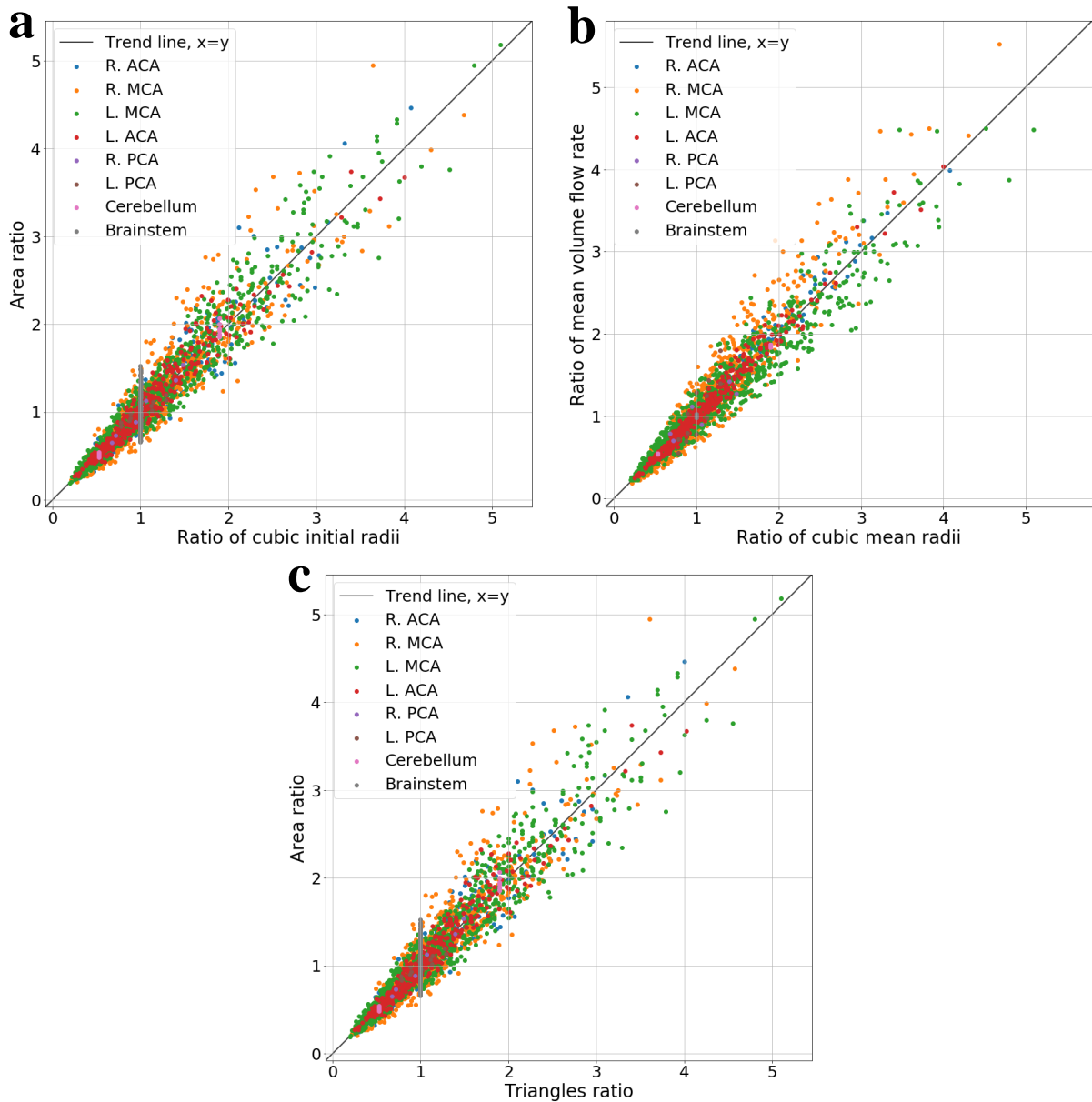
Figure 5: Relationships between perfusion territories within the same major region. (a) shows the fraction between cubed radii at the outlet and area on the pial surface. (b) shows the fraction between cubed radii at the outlet and the mean volume flow rate. (c) shows the fraction between the number of triangles of two clusters and their area. All figures show linear relationships.

The coupling algorithm essentially maps the pial surface to the nearest vessel. The main benefit from the coupling algorithm is that it ensures that the perfusion territories are sized correctly, see Figure 5. Shown in Figure 5 are ratios between various variables within regions of the brain. Every outlet is compared to every other outlet in a specific region of the brain. The ratios provide a way to compare the results of the model to the model assumptions. Figure 5a shows the relationship between the cubic radius and the area on the pial surface of the vessel outlets. Figure 5b shows the relationship between cubic radius and mean volume flow rates, see equation 14. Figure 5c shows the relation between the number of triangles and area on the surface mesh. The ratios display a linear relationship and any deviation from the linear relationship represents a deviation from the model assumptions.

The coupling method is graph based and works with any geometry and distance metric. Different scaling laws can be applied by changing the calculation of fractional area. A simple alternative to the coupling algorithm would be to map the surface to the nearest outlet. However, this can cause problems when some outlets are mapped to large areas of the surface and other are not mapped at all. The effect of different sized radii at the ends to the vessels cannot be ignored. Another way to estimate perfusion territories is based on calculating streamlines (42). However, this method is computationally expensive and can run into issues with large complicated geometries.
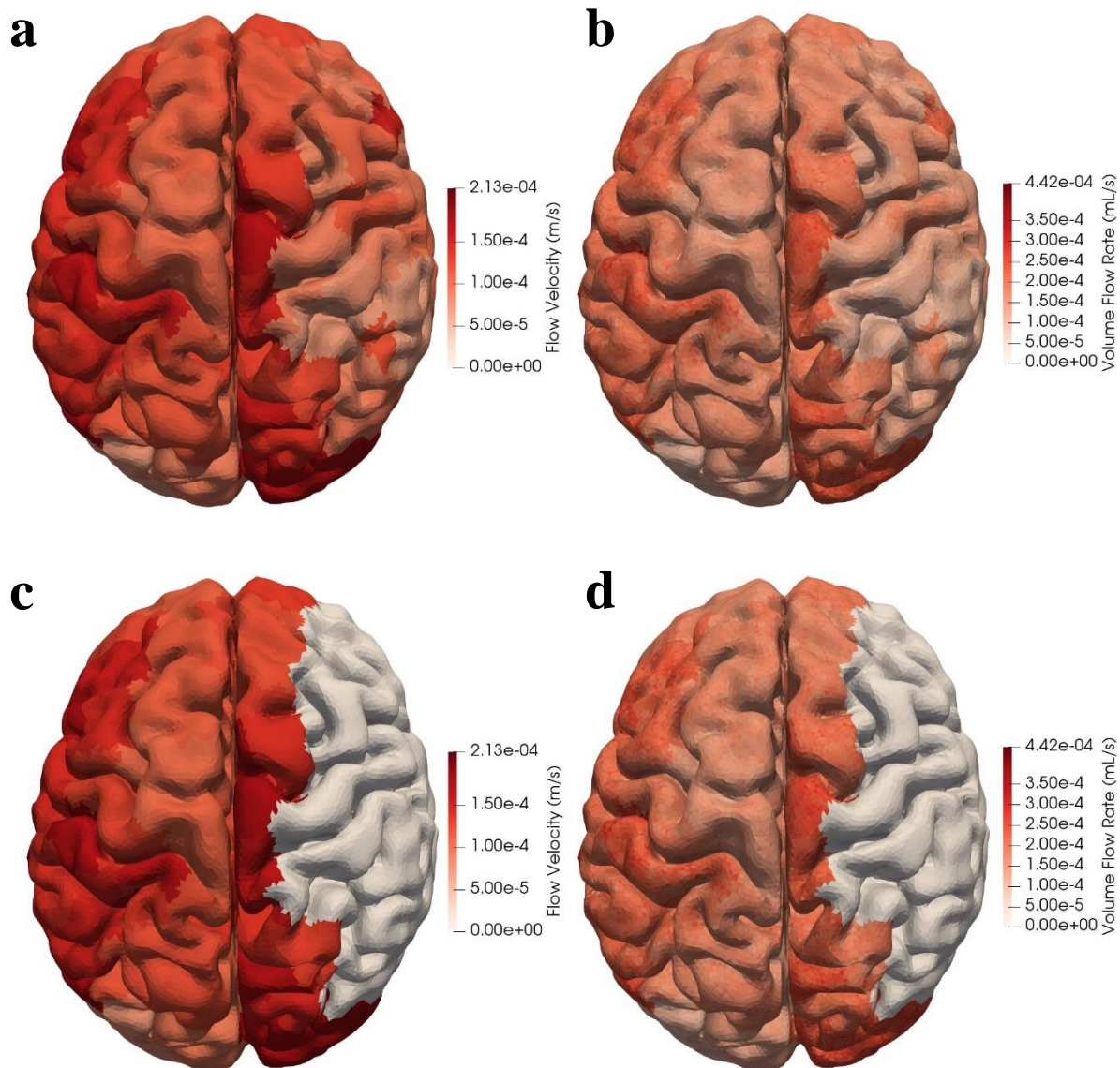

Figure 6: (a) Mean blood flow velocity at the pial surface for a healthy patient. The mean volume flowrate divided by the cluster area for each vessel outlet to the pial surface is shown. All values are within one order of magnitude of each other. (b) Volume flow rate on the mesh for a healthy patient. The volume flow rate at the outlet of the vessel is mapped to its cluster on the mesh. There are large differences between clusters as the outlet radii can differ significantly. (c) Flow velocity at the pial surface for a patient with a stroke. There is a clot in the right middle cerebral artery. Pressure after the clot is equal to that of the venous system and

flow is zero. (d) Volume flow rate at the pial surface for a patient with a stroke. Any vessel originating from the right middle cerebral artery has zero flow and their perfusion territories receive no blood.

The mapping of the pial surface to the outlets of the 1-D blood flow model is shown in Figure 4b. The volume flow rate at the outlets of the 1-D blood flow model is distributed evenly across its perfusion territory. Figure 6a shows the mean blood flow velocity at the pial surface and Figure 6b shows the mean volume blood flow rate at the pial surface. There are some differences in flow rate at the pial surface but all flow rates are within one order of magnitude. These differences are largely due to deviations from the assumed proportionality between radius and volume flow rate, equation 14 and Figure 5b. The surface mesh also does not capture all the complexity of the human brain and affects the distribution of the flow across the pial surface, Figures 5a and 5c. Improving the quality of the surface mesh and improving the surface mapping as well as validation of the mapping will be addressed in future work.

A clot can be modelled by introducing a reflective boundary condition at the boundary of the flow. This is achieved by enforcing a zero-pressure gradient, resulting in zero flow through the clot. Figure 6c shows the effect of a clot in the right middle cerebral artery on the velocity of flow at the pial surface. Figure 6d shows the effect of the same clot on the volume flow rate to the pial surface. The figures show that downstream of the clot there is no flow, leading to regions on the pial surface that lack flow. These are the areas where an infarct will start to form.

The framework presented here can be used to model blood flow to organs such as the brain. In addition, the mapping algorithm can be used to estimate perfusion territories for any organ as along as the appropriate distance metric is used. It is important to capture enough of the vasculature to be able to accurate predict pressure and flow rates. Patient-specific simulations are a challenge from a modelling as well as a data perspective. Obtaining correlated parameters as well as patient-specific segmentations is a major challenge for creating patient-specific simulations.

6 Conclusion

In silico trials can dramatically improve the process of development of medical devices, drugs and treatments. IST can reduce the cost and duration of running a trial by reducing the need for patients and speeding up testing. The INSIST consortium (43) aims to create an in silico trial for treatment of acute ischaemic stroke. The trial will include models of the patient population, arterial blood flow, tissue perfusion, metabolism, thrombosis and thrombolysis and thrombectomy. Here the arterial blood flow model and a method for estimating perfusion territories is presented. is to a tissue perfusion model for patient-specific simulations is presented. Image based patient-specific data on the anatomy of the circle of Willis is combined with literature data and models for vessel anatomy not visible in the images to create an extended model for each patient. An acute ischaemic stroke can be modelled as the blockage of flow at any point in the vasculature. Modelling stroke and predicting infarct volume requires the coupling of multiple models on different scales. A method to couple patient-specific blood flow models to a tissue perfusion model is presented. Blood flow to the pial surface can be approximated as steady if we accept a small error due to the loss of the time-dependent behaviour. Additional work remains, however, to be done on the incorporation of feedback between the blood flow model and the tissue perfusion model.

7 Data, code and materials

Patient-specific data is not available due to privacy regulations. The BraVa dataset is freely available from http://cng.gmu.edu/brava. Code and other materials are included as supplementary material.

8 Funding

9 Competing interests

The authors declare no conflict of interest.

10 Authors' contributions

R.M. Padmos has contributed to the design of the research, performed the research and written the paper. T.I. Józsa has contributed to the design of the research, contributed data and revised the paper. W.K. El-Bouri, S.J. Payne, and A.G. Hoekstra have contributed to the design of the research and revised the paper.

11 References

1. Wang H, Naghavi M, Allen C, Barber RM, Bhutta ZA, Carter A, et al. Global, regional, and national life expectancy, all-cause mortality, and cause-specific mortality for 249 causes of death, 1980–2015: a systematic analysis for the Global Burden of Disease Study 2015. Lancet [Internet]. 2016 Oct;388(10053):1459–544. Available from: https://linkinghub.elsevier.com/retrieve/pii/S0140673616310121

2. Gounis M, Narata AP, Valvassori L, Lugt A van der, Lingsma H, Jongejan L, et al. INSIST Clinical Focus Group Discussions at INSIST All hands workshop Milan – a Whitepaper. 2019;(April). Available from: https://www.insist-h2020.eu/images/Dissemination/INSIST_Clinical_Focus_Group_Meeting_at_INSIST__Milan_WhitePaper-version_01.pdf

3. Viceconti M, Henney A, Morley-Fletcher E. in silico Clinical Trials: How Computer Simulation will Transform the Biomedical Industry. Research and Technological Development Roadmap, Avicenna Consortium. Avicenna Consort. 2016;

4. Bradley P. The history of simulation in medical education and possible future directions. Med Educ [Internet]. 2006 Mar;40(3):254–62. Available from: http://doi.wiley.com/10.1111/j.1365-2929.2006.02394.x

5. Viceconti M, Hunter P. The Virtual Physiological Human: Ten Years After. Annu Rev Biomed Eng [Internet]. 2016 Jul 11;18(1):103–23. Available from: http://www.annualreviews.org/doi/10.1146/annurev-bioeng-110915-114742

6. Hoekstra AG, van Bavel E, Siebes M, Gijsen F, Geris L. Virtual physiological human 2016: translating the virtual physiological human to the clinic. Interface Focus [Internet]. 2018 Feb 6;8(1):20170067. Available from: http://rsfs.royalsocietypublishing.org/lookup/doi/10.1098/rsfs.2017.0067

7. Hoekstra AG, van de Vosse F, Röhrle O. The Virtual Physiological Human Conference 2016. J Comput Sci [Internet]. 2018 Jan;24:65–7. Available from:

https://linkinghub.elsevier.com/retrieve/pii/S1877750317313467

8.   Gray RA, Pathmanathan P. Patient-Specific Cardiovascular Computational Modeling: Diversity of Personalization and Challenges. J Cardiovasc Transl Res [Internet]. 2018 Apr 6;11(2):80–8. Available from: http://link.springer.com/10.1007/s12265-018-9792-2

9.   Gueyffier F, Strang CB, Berdeaux G, França LR, Blin P, Benichou J, et al. Contribution of Modeling Approaches and Virtual Populations in Transposing the Results of Clinical Trials into Real Life and in Enlightening Public Health Decisions. Therapie [Internet]. 2012 Jul;67(4):367–74. Available from: http://linkinghub.elsevier.com/retrieve/pii/S0040595716308526

10.   El-Bouri WK, Payne SJ. Multi-scale homogenization of blood flow in 3-dimensional human cerebral microvascular networks. J Theor Biol [Internet]. 2015;380:40–7. Available from: http://dx.doi.org/10.1016/j.jtbi.2015.05.011

11.   Jozsa T, El-Bouri W, Padmos R, Payne S, Hoekstra A. A cerebral circulation model for in silico clinical trials of ischaemic stroke [Details will be updated once accepted]. 2019;

12.   Mut F, Wright S, Ascoli GA, Cebral JR. Morphometric, geographic, and territorial characterization of brain arterial trees. Int j numer method biomed eng [Internet]. 2014 Jul;30(7):755–66. Available from: http://doi.wiley.com/10.1002/cnm.2627

13.   Wright SN, Kochunov P, Mut F, Bergamino M, Brown KM, Mazziotta JC, et al. Digital reconstruction and morphometric analysis of human brain arterial vasculature from magnetic resonance angiography. Neuroimage [Internet]. 2013 Nov;82:170–81. Available from: http://dx.doi.org/10.1016/j.neuroimage.2013.05.089

14.   Hartkamp NS, Petersen ET, De Vis JB, Bokkers RPH, Hendrikse J. Mapping of cerebral perfusion territories using territorial arterial spin labeling: techniques and clinical application. NMR Biomed [Internet]. 2013 Aug;26(8):901–12. Available from: http://doi.wiley.com/10.1002/nbm.2836

15.   Alastruey J, Parker KH, Peiró J, Byrd SM, Sherwin SJ. Modelling the circle of Willis to assess the effects of anatomical variations and occlusions on cerebral flows. J Biomech [Internet]. 2007 Jan 1 [cited 2018 Jan 31];40(8):1794–805. Available from: https://www.sciencedirect.com/science/article/pii/S0021929006002946

16.   Akgun V, Battal B, Bozkurt Y, Oz O, Hamcan S, Sari S, et al. Normal Anatomical Features and Variations of the Vertebrobasilar Circulation and Its Branches: An Analysis with 64-Detector Row CT and 3T MR Angiographies. Sci World J [Internet]. 2013;2013:1–7. Available from: http://www.hindawi.com/journals/tswj/2013/620162/

17.   Alastruey J, Parker KH, Sherwin SJ. Arterial pulse wave haemodynamics. 11th Int Conf Press Surges. 2012;(1):401–43.

18.   van de Vosse FN, Stergiopulos N. Pulse Wave Propagation in the Arterial Tree. Annu Rev Fluid Mech [Internet]. 2011;43(1):467–99. Available from: http://www.annualreviews.org/doi/abs/10.1146/annurev-fluid-122109-160730

19.   Milišić V, Quarteroni A. Analysis of lumped parameter models for blood flow simulations and their relation with 1D models. ESAIM Math Model Numer Anal [Internet]. 2004 Jul 15;38(4):613–32. Available from:

http://journals.cambridge.org/abstract_S0764583X05000166

20. Sherwin SJ, Franke V, Peiró J, Parker K. One-dimensional modelling of a vascular network in space-time variables. J Eng Math. 2003;47(3–4):217–50.

21. Boileau E, Nithiarasu P, Blanco PJ, Müller LO, Fossan FE, Hellevik LR, et al. A benchmark study of numerical schemes for one-dimensional arterial blood flow modelling. Int j numer method biomed eng [Internet]. 2015 Oct [cited 2015 Nov 16];31(10):1–33. Available from: http://www.ncbi.nlm.nih.gov/pubmed/26100764

22. Reymond P, Merenda F, Perren F, Ru D. Validation of a One-Dimensional Model of the Systemic Arterial Tree. Am J Physiol - Hear Circ Physiol. 2009;297:208–22.

23. Blanco PJ, Watanabe SM, Passos MARF, Lemos PA, Feijoo RA. An Anatomically Detailed Arterial Network Model for One-Dimensional Computational Hemodynamics. IEEE Trans Biomed Eng [Internet]. 2015 Feb;62(2):736–53. Available from: http://ieeexplore.ieee.org/document/6933913/

24. DeMers D, Wachs D. Physiology, Mean Arterial Pressure. In: StatPearls [Internet]. StatPearls Publishing; 2019.

25. Murray CD. The Physiological Principle of Minimum Work: I. The Vascular System and the Cost of Blood Volume. Proc Natl Acad Sci U S A [Internet]. 1926 Mar;12(3):207–14. Available from: http://www.ncbi.nlm.nih.gov/pmc/articles/PMC1084489/

26. Alastruey J, Moore SM, Parker KH, David T, Peiró J, Sherwin SJ. Reduced modelling of blood flow in the cerebral circulation: Coupling 1-D, 0-D and cerebral auto-regulation models. Int J Numer Methods Fluids [Internet]. 2008 Mar 20 [cited 2018 Feb 26];56(8):1061–7. Available from: http://doi.wiley.com/10.1002/fld.1606

27. Garcia-Gonzalez D, Jayamohan J, Sotiropoulos SN, Yoon S-H, Cook J, Siviour CR, et al. On the mechanical behaviour of PEEK and HA cranial implants under impact loading. J Mech Behav Biomed Mater [Internet]. 2017 May;69(January):342–54. Available from: http://dx.doi.org/10.1016/j.jmbbm.2017.01.012

28. Hartkamp NS, Petersen ET, Chappell MA, Okell TW, Uyttenboogaart M, Zeebregts CJ, et al. Relationship between haemodynamic impairment and collateral blood flow in carotid artery disease. J Cereb Blood Flow Metab [Internet]. 2018 Nov 4;38(11):2021–32. Available from: http://journals.sagepub.com/doi/10.1177/0271678X17724027

29. Mutsaerts HJMM, van Dalen JW, Heijtel DFR, Groot PFC, Majoie CBLM, Petersen ET, et al. Cerebral Perfusion Measurements in Elderly with Hypertension Using Arterial Spin Labeling. Jiang Q, editor. PLoS One [Internet]. 2015 Aug 4;10(8):e0133717. Available from: http://dx.plos.org/10.1371/journal.pone.0133717

30. Tatu L, Moulin T, Bogousslavsky J, Duvernoy H. Arterial territories of the human brain: cerebral hemispheres. Neurology [Internet]. 1998 Jun;50(6):1699–708. Available from: https://www.karger.com/Article/FullText/333602

31. Karch R, Neumann F, Neumann M, Schreiner W. Staged Growth of Optimized Arterial Model Trees. Ann Biomed Eng [Internet]. 2000 May;28(5):495–511. Available from: http://link.springer.com/10.1114/1.290

32. Karch R, Neumann F, Neumann M, Schreiner W. A three-dimensional model for arterial tree representation, generated by constrained constructive optimization.

Comput Biol Med [Internet]. 1999 Jan;29(1):19–38. Available from: http://linkinghub.elsevier.com/retrieve/pii/S0010482598000456

33. Schreiner W, Buxbaum PF. Computer-optimization of vascular trees. IEEE Trans Biomed Eng [Internet]. 1993 May;40(5):482–91. Available from: http://ieeexplore.ieee.org/document/243413/

34. Hayashi K, Handa H, Nagasawa S, Okumura A, Moritake K. Stiffness and elastic behavior of human intracranial and extracranial arteries. J Biomech [Internet]. 1980 Jan;13(2):175–84. Available from: https://linkinghub.elsevier.com/retrieve/pii/0021929080901918

35. Michel E, Zernikow B. Gosling's Doppler Pulsatility Index Revisited. Ultrasound Med Biol [Internet]. 1998 May;24(4):597–9. Available from: https://linkinghub.elsevier.com/retrieve/pii/S0301562998000246

36. Kim Y, Lee H, An SA, Yim B, Kim J, Kim OJ, et al. The effect of pulsatility index on infarct volume in acute lacunar stroke. Yonsei Med J. 2016;57(4):950–5.

37. Kidwell CS, El-Saden S, Livshits Z, Martin NA, Glenn TC, Saver JL. Transcranial Doppler Pulsatility Indices as a Measure of Diffuse Small-Vessel Disease. J Neuroimaging [Internet]. 2001 Jul;11(3):229–35. Available from: http://doi.wiley.com/10.1111/j.1552-6569.2001.tb00039.x

38. Xu T-Y, Staessen JA, Wei F-F, Xu J, Li F-H, Fan W-X, et al. Blood Flow Pattern in the Middle Cerebral Artery in Relation to Indices of Arterial Stiffness in the Systemic Circulation. Am J Hypertens [Internet]. 2012 Mar 1;25(3):319–24. Available from: http://dx.doi.org/10.1038/ajh.2011.223/nature06264

39. Ghorbani A, Ahmadi M, Shemshaki H. The value of transcranial Doppler derived pulsatility index for diagnosing cerebral small-vessel disease. Adv Biomed Res [Internet]. 2015;4(1):54. Available from: http://www.advbiores.net/text.asp?2015/4/1/54/151574

40. Mitchell GF, van Buchem MA, Sigurdsson S, Gotal JD, Jonsdottir MK, Kjartansson Ó, et al. Arterial stiffness, pressure and flow pulsatility and brain structure and function: the Age, Gene/Environment Susceptibility – Reykjavik Study. Brain [Internet]. 2011 Nov;134(11):3398–407. Available from: https://academic.oup.com/brain/article-lookup/doi/10.1093/brain/awr253

41. Okell TW, Chappell MA, Kelly ME, Jezzard P. Cerebral Blood Flow Quantification Using Vessel-Encoded Arterial Spin Labeling. J Cereb Blood Flow Metab [Internet]. 2013 Nov 7;33(11):1716–24. Available from: http://dx.doi.org/10.1038/jcbfm.2013.129

42. Blanco PJ, de Queiroz RAB, Feijóo RA. A computational approach to generate concurrent arterial networks in vascular territories. Int j numer method biomed eng [Internet]. 2013 May;29(5):601–14. Available from: http://doi.wiley.com/10.1002/cnm.2547

43. In Silico trials for acute ischemic stroke [Internet]. Available from: https://www.insist-h2020.eu/